AGU PUBLICATIONS

Paleoceanography

RESEARCH ARTICLE

10.1002/2013PA002598

Assessing divergent SST behavior during the last 21 ka derived from alkenones and *G. ruber*-Mg/Ca in the equatorial Pacific

Axel Timmermann[1], Julian Sachs[2], and Oliver Elison Timm[3]

[1]International Pacific Research Center, SOEST, University of Hawai'i at Mānoa, Honolulu, Hawaii, USA, [2]School of Oceanography, University of Washington, Seattle, Washington, USA, [3]Department of Atmospheric and Environmental Sciences, State University of New York at Albany, Albany, New York, USA

Key Points:
- Tropical Pacific alkenone SSTs are biased toward boreal winter
- Tropical Pacific Mg/Ca SST of *G. ruber* are biased toward boreal summer
- Alkenone and Mg/Ca data can be used to obtain annual mean and seasonal amplitude

Correspondence to:
A. Timmermann,
axel@hawaii.edu

Citation:
Timmermann, A., J. Sachs, and O. Elison Timm (2014), Assessing divergent SST behavior during the last 21 ka derived from alkenones and *G.ruber*-Mg/Ca in the equatorial Pacific, *Paleoceanography*, *29*, 680–696, doi:10.1002/2013PA002598.

Received 16 DEC 2013
Accepted 31 MAY 2014
Accepted article online 6 JUN 2014
Published online 30 JUN 2014

Abstract Equatorial Pacific SST reconstructions derived from Mg/Ca ratios in planktonic foraminifera *Globigerinoides ruber* and from alkenone-producing coccolithophorids record different trends throughout the Holocene and the last deglaciation. We set forth the hypothesis that their diverging behavior may be related to different seasonal sensitivities which result from the annually varying production rates of alkenone-producing coccolithophorids and of *G. ruber*. Using a series of transient paleoclimate model simulations forced with the time-varying forcing history over the last 21 ka, a good qualitative agreement is found between simulated boreal winter temperatures and alkenone-SST reconstructions as well as between simulated boreal summer temperatures and reconstructed Mg/Ca-based SST variations. Pronounced features in the reconstructions that can be readily explained by the conjectured seasonal biases include the mismatch in middle-to-late Holocene temperature trends and the different onsets of deglacial climate change in the eastern equatorial Pacific. The analysis presented here further suggests that through combinations of Mg/Ca and alkenone SST reconstructions information can be gained on annual mean temperature changes and the amplitude of the seasonal cycle in SST. Our study concludes by discussing potential weaknesses of the proposed model-derived seasonal bias interpretation of tropical Pacific SST proxies in terms of present-day core-top data, sediment trap studies, and satellite-based observations of chlorophyll.

1. Introduction

There has been an explosion in recent years of the application of multiple climate proxies at a single location in order to improve the confidence of climate reconstructions. In many instances, this has led to the awkward situation of having to argue for the merits of one proxy, and against the merits of another, when they do not provide the same result. This choice is all-too-often not driven by scientific evidence. But without sufficient information about the geographic-specific depth and seasonal habitats of the organisms that record paleoclimate signals, the biological influence on proxies (both the biochemical mechanism for the signal and the so-called vital effects), diagenetic alteration of signals, and depositional and postdepositional processes (such as lateral advection of particles and bioturbation), there is often little choice than to pick one proxy result over another in order to develop an interpretable climate time series. If one starts with the assumption that two proxies of the same climate parameter, such as SST, accurately record sea surface temperature (SST), and the time series of SST resulting from the application of the two proxies differ, then it is necessary to explore mechanisms by which two SST series from the same location can differ substantially and what aspects of SST are actually being captured.

Given two very different proxies, such as the alkenone unsaturation ratio $U^{k'}_{37} = C_{37:2}/(C_{37:2} + C_{37:3})$ ($C_{37:2}$ and $C_{37:3}$ represent concentrations of diundersaturated and triundersaturated alkenones) from lipids produced by coccolithophorid phytoplankton, and Mg/Ca ratios in the shells of one species of planktonic foraminifera, one should expect different temperature series unless the two organisms inhabit the same water depth at the same time of the year—an unlikely situation. A recent modeling study [*Fraile et al.*, 2009] of the seasonality of different plankton species has further demonstrated that the seasonal preferences may even change, as the climate system progresses from glacial to interglacial conditions. This will further complicate the interpretation of Mg/Ca and alkenone-based temperature reconstructions. Here we evaluate divergent trends in SST histories during the last ~25 ka provided by alkenones and Mg/Ca in *G. ruber* from the eastern and western equatorial Pacific.

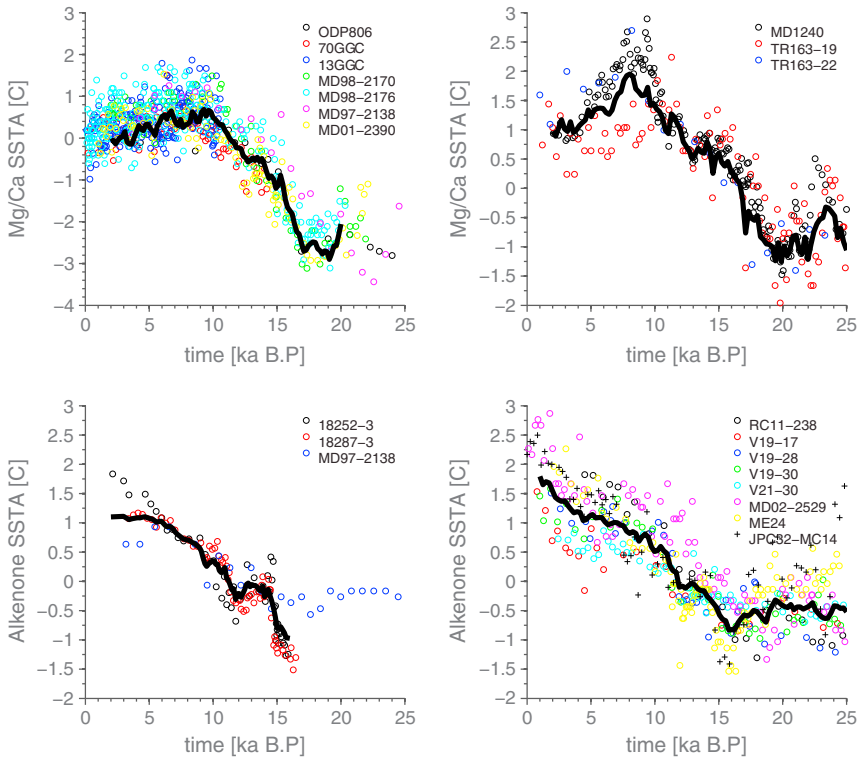

Figure 1. (top left) Western equatorial Pacific SST based on Mg/Ca data of *G. ruber* from cores ODP806, 70GGC, 13GGC, MD98-2170, MD98-2176, MD97-2138, and MD01-2390; the mean of the splined Mg/Ca Sea Surface Temperature Anomalies (SSTA) data sets is indicated as a thick black line. (top right) Eastern equatorial Pacific SST based on Mg/Ca data of *G. ruber* from cores MD2140, TR163-19, and TR163-22; the mean of the splined Mg/Ca SSTA data sets is indicated as a thick black line. (bottom left) Western equatorial Pacific SST based on alkenone unsaturation data from cores 18252-3, 18287-3, and MD97-2138; the mean of the splined alkenone SSTA data sets is indicated as a thick black line. (bottom right) Eastern equatorial Pacific SST based on alkenone unsaturation data from cores RC11-238, V19-27, V19-28, V19-30, V21-30, MD02-2529, ME24, and JPC32-MC14; the mean of the splined alkenone SSTA data sets is indicated as a thick black line.

Whereas alkenone-based SSTs in the eastern and western equatorial Pacific indicate continuous warming throughout the Holocene, with a magnitude similar to that of the deglacial SST change, *G. ruber* Mg/Ca series usually indicate cooling from 8 ka B.P. to the present (see Figure 1). Furthermore, alkenone-based deglacial warming in the eastern equatorial Pacific starts around 16–15 ka B.P. (Figure 1, bottom right), in contrast to the much earlier warming seen in the Mg/Ca SST data. In fact, the alkenone-derived warming starts at a time when the Mg/Ca data have already attained about half of their glacial-interglacial amplitude (Figure 1, top right). Understanding the causes for these discrepancies will give us a deeper understanding of the controlling factors of late Pleistocene and Holocene climate change.

The key hypothesis that will be explored is that some first-order discrepancies between Mg/Ca and alkenone-based temperature proxies can be reconciled by invoking different bulk seasonal sensitivities. Potential seasonal biases of SST proxy data have already been discussed in previous studies [e.g., *Nürnberg et al.*, 2000; *Ashkenazy and Tziperman*, 2006; *Steinke et al.*, 2008; *Leduc et al.*, 2010; *Schneider et al.*, 2010; *Harada et al.*, 2012; *Wang et al.*, 2013; *Rosell-Melé and Prahl*, 2013] by (i) identifying seasonal preferences of coccolithophores and *G. ruber* in different regions and (ii) by comparing temperature reconstructions with the orbital insolation trends that match the seasonal preferences of the corresponding proxy [*Leduc et al.*, 2010; *Schneider et al.*, 2010].

Here we will further test this hypothesis by analyzing satellite chlorophyll data, $U^{k'}_{37}$, sediment trap data, core-top data and transient climate modeling experiments covering the past 21 ka.

The paper is organized as follows. Following a critical assessment of the equatorial Pacific SST proxy data, seasonal and depth habitats of coccolithophores and *G. ruber* and core-top alkenone/SST correlations (section 2), we will present a paleoproxy data/model comparison that is based on transient model solutions

Table 1. Alkenone SST Reconstructions Used in This Study

Proxy	Core	Location	Depth (m)	Reference
Alkenone	MD97-2138	1.25°S, 146.15°E	1960	*de Garidel-Thoron et al.* [2007]
Alkenone	18252-3	9.23°N, 109.4°W	1273	*Kienast et al.* [2001]
Alkenone	18287-3	5.7°N, 110.7°E	598	*Kienast et al.* [2001]
Alkenone	RC11-238	1.5°S, 85.5°W	2573	*Koutavas and Sachs* [2008]
Alkenone	V19-27	0.28°S, 82.1°W	1373	*Koutavas and Sachs* [2008]
Alkenone	V19-28	2.4°S, 84.65°W	2720	*Koutavas and Sachs* [2008]
Alkenone	V19-30	3.4°S, 83.5°W	3091	*Koutavas and Sachs* [2008]
Alkenone	V21-30	1.2°S, 89.7°W	617	*Koutavas and Sachs* [2008]
Alkenone	MD02-2529	8.2°N, 84.1°W	1619	*Leduc et al.* [2007]
Alkenone	ME0005A-24JC	1.5°N, 86.5°W	2941	*Kienast et al.* [2006]
Alkenone	MC14	4.8°N, 77.6°W	884	*Pahnke et al.* [2007]
Alkenone	JPC32	4.6°N, 77.9°W	2200	*Pahnke et al.* [2007]
Alkenone	ME0005-27JC	1.8°S, 82.8°W	2203	*Kienast et al.* [2006]
Alkenone	TR163-19P	2.2°N, 91°W	2348	*Kienast et al.* [2006]

obtained with an earth system model of intermediate complexity (section 3). The paper concludes with a summary and discussion (section 4).

2. Proxy Data

To develop a better understanding of the discrepancies of $U^{k'}_{37}$-SST and Mg/Ca-based SST reconstructions on glacial/interglacial time scales, we focus on a compilation of cores from the western and eastern equatorial Pacific (see Tables 1 and 2), shown in Figure 1.

To highlight some of the common and most robust features in these records, we have composited the alkenone (using 18252-3, 18287-3, and MD97-2138 for the western equatorial Pacific (WEP) and RC11-238, V19-27, V19-28, V19-30, V21-30,MD02-2529, ME24, and JPC32-MC14 for the eastern equatorial Pacific (EEP)) (Figure 1, bottom, black lines) as well as the Mg/Ca records (using ODP806, 70GGC, 13GGC, MD98-2170, MD98-2176, MD97-2139, and MD01-2390 for the WEP and MD1240, TR163-19, and TR163-22 for the EEP) (Figure 1, top, black lines) by linearly interpolating the proxy data in time and averaging the resulting time series for the respective proxies and for the respective regions.

2.1. Seasonal Biases Due to Spatial Sampling

Before analyzing the individual SST proxy records and comparing them to transient climate model simulations, it is important to review the spatiotemporal structure of near-surface productivity and SSTs under present-day conditions. Here we use the Sea-viewing Wide Field-of-view Sensor (SeaWiFS) ocean color-derived chlorophyll [e.g., *McClain et al.*, 1998; *Yoder and Kennelly*, 2003] as a proxy for primary productivity. This data set is a monthly climatology obtained for the period January 2003 to December 2006 and averaged on a 0.25° latitude/longitude grid map. We compare the chlorophyll data to the SST climatology obtained from the Advanced Very High Resolution Radiometer (AVHRR) satellite product averaged from January 1985 to December 2002 [*Reynolds et al.*, 2007], to evaluate the degree of spatial heterogeneity in productivity and SST by calculating the month at which chlorophyll concentrations (SSTs) attain their

Table 2. Mg/Ca SST Reconstructions Used in This Study

Proxy	Core	Location	Depth	Reference
Mg/Ca *G. ruber*	TR163-19	2.2°N, 91°W	2348	*Lea et al.* [2000]
Mg/Ca *G. ruber*	ODP806	0.3°N, 159°E	2520	*Medina-Elizalde and Lea* [2005]
Mg/Ca *G. ruber*	TR163-22	0.5°N, 92.3°W	2830	*Lea et al.* [2006]
Mg/Ca *G. ruber*	70GGC	3.55°S, 119.3°E	482	*Linsley and Rosenthal* [2010]
Mg/Ca *G. ruber*	13GGC	7.45°S, 115.2°E	2924	*Linsley and Rosenthal* [2010]
Mg/Ca *G. ruber*	MD98-2170 GGC	10.6°S, 125.4°E	832	*Stott et al.* [2007]
Mg/Ca *G. ruber*	MD98-2176	5°S, 133.3°E	2382	*Stott et al.* [2004]
Mg/Ca *G. ruber*	MD97-2138	1.25°N, 146.1°E	1960	*de Garidel-Thoron et al.* [2007]
Mg/Ca *G. ruber*	MD01-2390	6.6°N, 113.5°E	1545	*Steinke et al.* [2008]
Mg/Ca *G. ruber*	ODP 1240	0°N, 86.5°W	2921	*Pena et al.* [2008]

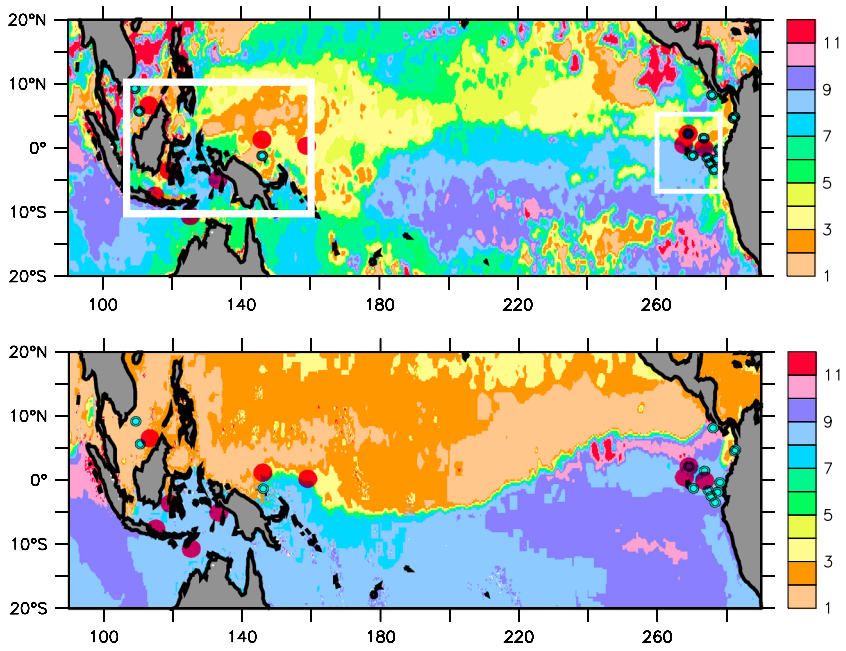

Figure 2. (top) Month of maximum chlorophyll concentration from the SeaWiFS ocean color satellite climatology [*McClain et al.*, 1998; *Yoder and Kennelly*, 2003]. (bottom) Month of minimum SST obtained from the AVHRR satellite SST climatology. Cyan (red) circles indicate core locations of alkenone (Mg/Ca) SST reconstructions.

maximum (minimum) values. Figure 2 (top) reveals the high degree of spatial and seasonal complexity of chlorophyll concentrations and, by extension, primary productivity. Large gradients for instance in the northeastern tropical Pacific indicate that on scales of less than 1000 km productivity can switch from a spring-dominated regime to a fall-dominated regime. It is important to note that the month of coldest SST in the equatorial Pacific does not follow the seasonal march of the Sun across the equator. Eastern equatorial Pacific sites (Figure 2) both from the Northern and Southern Hemisphere exhibit the lowest SST in boreal fall to winter. The eastern equatorial Pacific data locations within 5° of the equator (see cyan and red circles in Figure 2 and Table 1) have a similar seasonal cycle in SST (Figure 3, top right), irrespective of their positions north or south of the equator. In contrast, a strong hemispheric gradient exists for chlorophyll concentrations in the eastern equatorial Pacific (120°W–90°W). In other words, the season of maximum chlorophyll concentration and, by extension, primary productivity does not necessarily coincide with the season of minimum SST. This is further exemplified in the western to central equatorial Pacific, east of Papua New Guinea, and in the South Pacific Convergence Zone area (Figures 2 and 3). These results challenge the use of SST climatologies as a simple proxy for surface productivity.

In our compilation of $U^{k'}_{37}$ (Table 1) and Mg/Ca-based temperature reconstructions (Table 2), seasonal biases may occur in a composite record (Figure 1), if the majority of the SST data came from regions with a productivity maximum in a particular season and if productivity maxima were related to coccolithophore and foraminiferal abundances and fluxes. The spatial inhomogeneity is further illustrated for our site locations in Figure 2. We calculated the average of normalized satellite chlorophyll concentrations for all the core locations in the eastern equatorial Pacific (bottom right) and western equatorial Pacific (bottom left) with alkenone (red) and Mg/Ca (blue) records (see Tables 1 and 2 and Figure 1, circles). The alkenone data locations in the western equatorial Pacific are characterized by strong boreal winter blooms (Figure 3, bottom left), corresponding to lower temperatures (Figure 3, top left). A clear boreal summer/fall preference can be found for the Mg/Ca data locations in the eastern equatorial Pacific, consistent with lower SSTs (Figure 2, top right). The situation for the Mg/Ca data locations in the western Pacific and the $U^{k'}_{37}$ data in the eastern Pacific is less clear. In the former an early spring and late summer peak dominates the chlorophyll signal, whereas in the latter we find only a weak seasonal dependence in chlorophyll, in spite of a very pronounced seasonal cycle in SST.

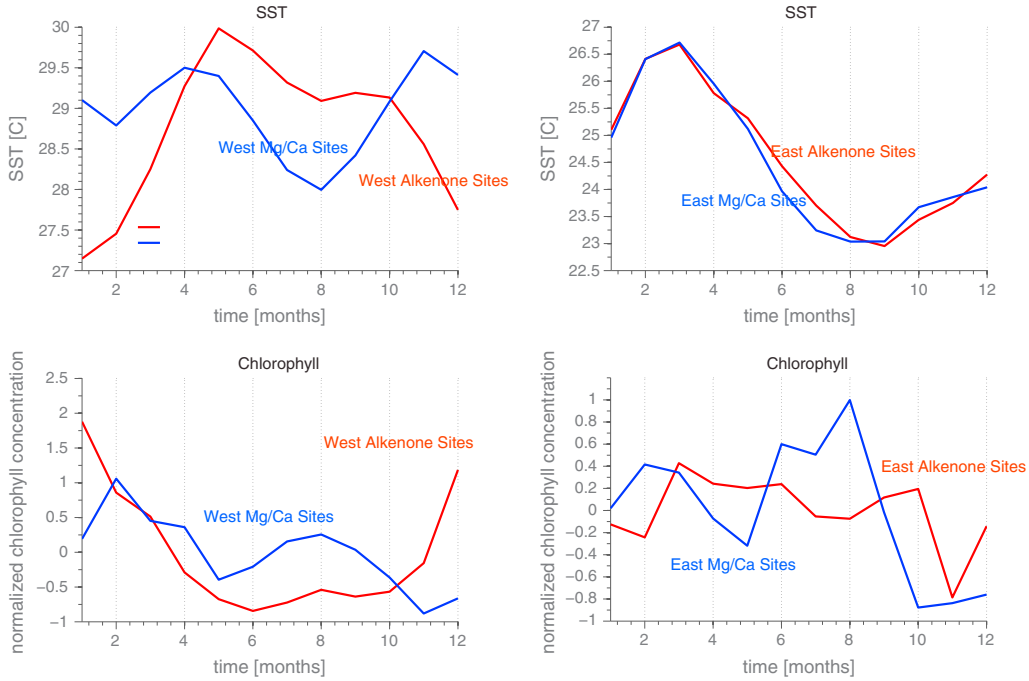

Figure 3. (top left) Averaged seasonal cycle of SST at sites with alkenone data (red) and Mg/Ca data (blue) (Table 1) in the western equatorial Pacific. SST is obtained from the AVHRR data set. (top right) Averaged seasonal cycle of SST at sites with alkenone data (red) and Mg/Ca data (blue) (Table 1) in the eastern equatorial Pacific. (bottom left) Average of normalized chlorophyll concentrations from the SeaWiFS data for alkenone (red) and Mg/Ca (blue) locations (see Table 1). (bottom right) The same as bottom left but for the eastern equatorial Pacific.

This analysis demonstrated that the spatial heterogeneity of seasonal chlorophyll maxima, and by extension, productivity maxima, may further complicate the attribution of seasonal biases of aggregated (spatially combined) alkenone and Mg/Ca temperature reconstructions.

2.2. Proxy-Dependent Seasonal Biases

A more detailed view of potential seasonal biases of Mg/Ca and alkenone-based temperature reconstructions at single locations has been obtained from sediment trap studies. Figure 4 shows the fluxes of *G. ruber* in the Panama basin (top left) [*Thunell and Reynolds*, 1984] and the satellite-derived chlorophyll concentrations at the sediment trap site (bottom left). Although chlorophyll concentrations, and inferred primary productivity, peak in boreal spring, the largest flux of *G. ruber* is observed in boreal summer. A lag in the population of zooplankton grazers (e.g., foraminifera) relative to primary producers (e.g., coccolithophorids) is commonly observed in the ocean, as is a lag in the sinking flux of plankton relative to the standing stock, so this is not surprising. The situation for Mg/Ca in the western equatorial Pacific, namely, in the South China Sea is a little bit more difficult to interpret. Whereas *Tian et al.* [2005] report maximum fluxes of *G. ruber* that peak on average from December to March during the season of maximum chlorophyll concentrations, another South China Sea sediment trap about 600 km away documents peak productivities in April and October [*Wan et al.*, 2010]. Whether such discrepancies represent the patchiness of phytoplankton blooms or the large effects of interannual monsoon variability is still an open question.

A better correspondence is found between the abundance of coccolithophores (Figure 4, top) and chlorophyll concentrations (Figure 4, bottom right) in the South China Sea [*Chen et al.*, 2007]. A very strong boreal winter peak in both suggests that $U^{k'}_{37}$-based temperature reconstructions, at least in the vicinity of the sediment trap, are likely to exhibit a winter bias. Other studies in the tropical Pacific [*Brown and Yoder*, 1994; *Wiesner et al.*, 1996; *Ziveri and Thunell*, 2000; *Harada et al.*, 2001] also discuss a possible boreal winter preference for alkenone-producing coccolithophorids. It has to be noted here that alkenone fluxes have been observed to peak during El Niño events in the Baja California Sur region [*Hernández-Becerril et al.*, 2007; *Silverberg et al.*, 2004], which may be interpreted to indicate a potential bias toward warm conditions. However, El Niño situations are very different from just an enhanced annual cycle, as they can be accompanied by major changes of thermocline depth, upwelling, and nutrient regimes. Moreover, with El Niño

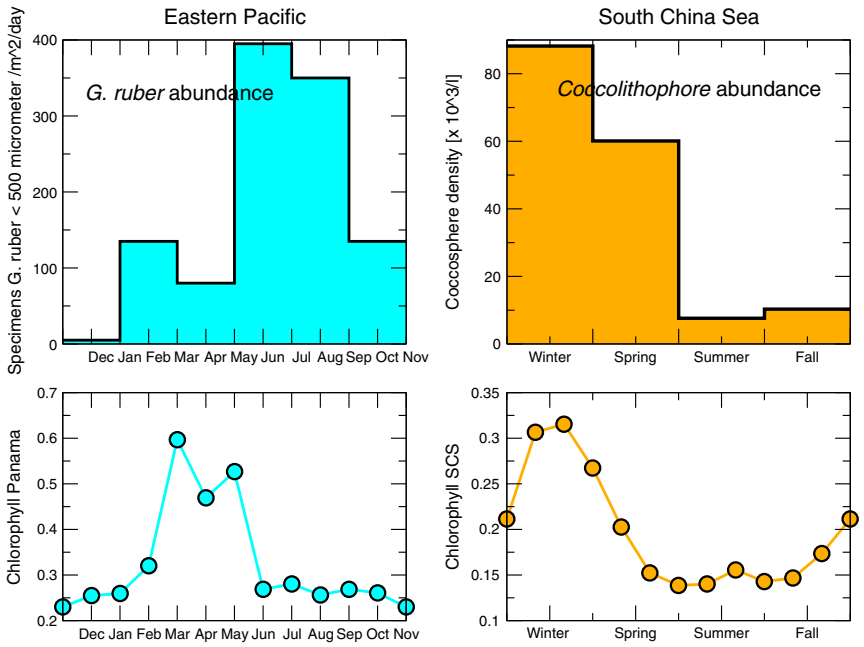

Figure 4. (top left) Bimonthly flux patterns for *G. ruber* in the Panama Basin, eastern equatorial Pacific [*Thunell and Reynolds*, 1984], measured at about 900 m depth. (top right) Seasonal coccolithophorid fluxes in the South China Sea from *Chen et al.* [2007]. The maximum flux of coccolithophorids occurs in boreal winter. In addition, the alkenone-producing species *E. huxleyi* and *G. oceanica* predominate the assemblage during that season (not shown). (bottom left) Mean climatological cycle of chlorophyll concentrations in the Panama Basin at the location of the sediment trap of *Thunell and Reynolds* [1984] derived from SeaWiFS ocean color data. (bottom right) Mean climatological cycle of chlorophyll concentrations in the South China Sea.

conditions peaking preferentially during boreal winter [*Stein et al.*, 2011], any inferred seasonal bias from this observation may be regarded as ambiguous.

Taken together, the studies discussed above further motivate the possibility for a strong seasonal modulation in regional coccolithophore abundances in the equatorial Pacific. This also suggests that the water temperatures, captured by the alkenone unsaturation index, are likely to be seasonally weighted, as hypothesized in numerous other studies.

2.3. Correlation of Core-Top Alkenone Data With SST

Many paleoproxy studies [e.g., *Müller et al.*, 1998; *Rosell-Melé et al.*, 2004; *Kienast et al.*, 2012; *Conte et al.*, 2006] have used the assumption that a high spatial correlation between core-top $U^{k'}_{37}$ values and the annual mean SST implies that alkenone data actually represent annual mean SSTs. Using a recent compilation of 123 EEP alkenone core-top data [*Kienast et al.*, 2012] and a present-day long-term SST climatology [*Reynolds et al.*, 2002] sampled at the core locations, we test the statistical stringency of this inference. Figure 5 (top) shows the pattern correlation between monthly mean climatological SST and the alkenone-based SST reconstructions. We find values of > 0.79 for all months, indicating that the overall SST pattern, except for an offset, remains relatively stable during the course of the year. Highest values, exceeding even the correlation with annual mean SST, are found for the month of June.

In order to compare the correlations amongst each other and determine statistically significant differences, we first transform the correlation values into Fisher's Z-score. Thereafter, the Z-scores are compared following *Cohen and Cohen* [1983] to obtain a corresponding two-tailed *p* value. The specific null hypothesis we are testing is "The pattern correlation between core top alkenone-based SSTs and annual mean SST equals the correlation between core top $U^{k'}_{37}$-based SSTs and longterm monthly mean SST." The results of this hypothesis testing are shown in Figure 5 (bottom). We find that we can reject the null hypothesis with high confidence ($> 90\%$) for the months of February and March. However, for all other months, the correlation coefficient is statistically indistinguishable from the annual mean correlation. It should be noted here that the lower alkenone/SST core-top correlations during February and March seem to be at odds with the

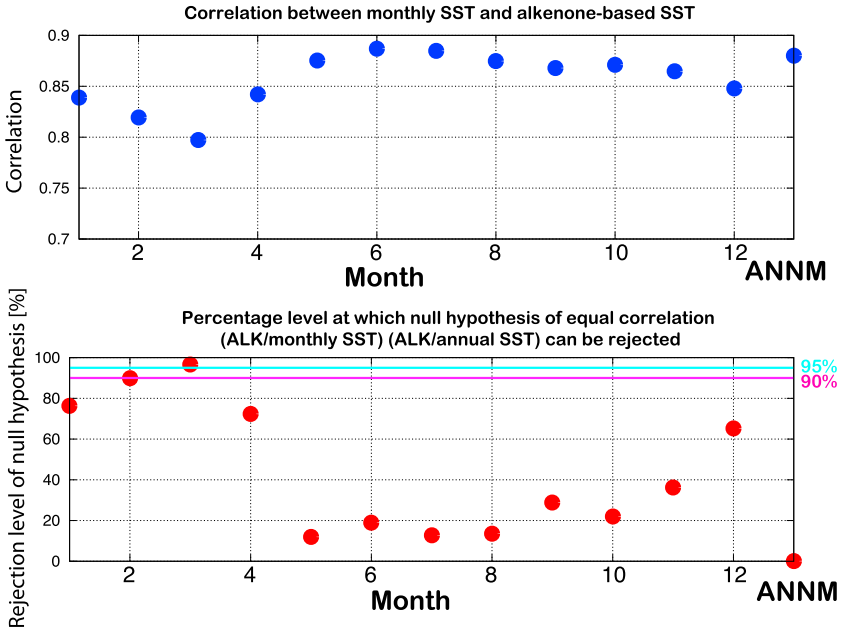

Figure 5. (top) Monthly spatial correlation between EEP core-top alkenone values from 123 sites [*Kienast et al.*, 2012] and present-day climatological SST. ANNM represents the annual mean. (bottom) Significance level (percent) at which the null hypothesis that a monthly SST/alkenone correlation is statistically different from the annual mean SST/alkenone correlation can be rejected. Results are based on Fisher's Z-scores.

finding of higher coccolithophore abundances in some equatorial Pacific locations [e.g., *Harada et al.*, 2001; *Chen et al.*, 2007], such as the western tropical Pacific (see, e.g., Figure 4). A more in-depth analysis of this mismatch would have to take into account the fact that sedimentation rates in the eastern equatorial Pacific are very low (~2 cm/ka) and that alkenone core-top data may represent averages over hundreds to thousands of years, rather than the just the present-day conditions.

This suggests that from a statistical point of view alkenone-based SST in the EEP could be interpreted as representing annual mean SST, or any other month (except February and March), or combinations thereof. Thus, the high correlation between alkenone-derived core-top SSTs and observed annual mean SST is not a sufficient criterion for an annual mean interpretation of alkenone data.

Another issue worth noting here is that a high spatial correlation between two different fields (e.g., alkenone and annual mean SST) does not necessarily imply a high temporal correlation between alkenone and annual mean SSTs, unless the spatial mean state pattern of SST is similar to the leading patterns of variability on the time scale under consideration.

2.4. Orbital-Scale Variations of Alkenone SSTs in the Equatorial Pacific

Returning now to the averaged $U^{k'}_{37}$-based SST indices in the EEP (Figure 1, bottom right), we find that the deglacial warming started around 16 ka B.P. which is ~2 ka after atmospheric CO_2 concentrations began to rise from glacial to interglacial values [*Monnin et al.*, 2001; *Lüthi et al.*, 2008]. This warming continued monotonically into the late Holocene. The Holocene trend of about 1°–3°C is comparable to the magnitude of deglacial warming between 21 and 11 ka B.P. Similar features can be observed for the WEP (Figure 1, bottom left). The wide variety of depositional settings, including depth and accumulation rate, surface, and abyssal circulations, unique to each core and the fact that the warming during Termination I (19–11 ka B.P.) and the Holocene are well reproduced by the composites of alkenone data from cores in the EEP and WEP (thick back lines in Figure 1, bottom) ensures that the signal is not the result of diagenesis or postdepositional processes, such as bioturbation or sediment advection. While there is still considerable scatter among the alkenone data from the EEP, all records show very similar orbital-scale variations that track the composite index. This finding virtually excludes the possibility that the long-term evolution in each core is determined by local processes such as advection of alkenones on the seafloor or in surface currents. Possible explanations for the quasi-monotonic warming trend in $U^{k'}_{37}$ SST records across the equatorial Pacific during the last 21 ka are (i) the mean annual temperature of surface waters throughout the equatorial Pacific increased,

(ii) the season that the alkenone-producing coccolithophorids lived had warmed continuously, (iii) the alkenone producers gradually moved to shallower depths in the water column, or (iv) the coccolithophorid season of growth became increasingly the warm season throughout the Holocene at the expense of the cold season, or combinations thereof. To address this question we will briefly review recent sediment trap studies.

The primary alkenone producers in the tropical Pacific are the coccolithophorids *Emiliania huxleyi* and *Gephyrocapsa oceanica* [*Bentaleb et al.*, 2002; *Ohkouchi et al.*, 1999; *Okada and Honjo*, 1973]. As photo-autotrophs, the depth habitat of these and other coccolithophorids is presumed confined to the euphotic zone [*Okada and Honjo*, 1973]. Consistent with that assumption, *Ohkouchi et al.* [1999] reanalyzed the data of *Okada and Honjo* [1973] and found that *E. huxleyi* and *G. oceanica* were most abundant between 0 and 100 m from 15°N to 10°S along the 155°W meridian. This conclusion is consistent with *Bentaleb et al.* [2002] who analyzed suspended particulate samples from the surface mixed layer of the western tropical and subtropical Pacific Ocean. Fewer studies on the depth habitat of coccolithophorids in the eastern equatorial Pacific exist but *E. huxleyi* is thought to inhabit the upper euphotic zone there [*Martinez et al.*, 2006]. *Ohkouchi et al.* [1999] further found that core-top SST derived from alkenone unsaturation indices in the central (155°W) and western (175°E) tropical Pacific tracked present-day surface annual mean mixed layer temperatures reasonably well. However, as discussed in section 2.3 high spatial correlations between core-top $U^{k'}_{37}$ data and annual mean mixed layer temperatures do not necessarily imply that alkenone data represent annual mean conditions. In fact, *Müller et al.* [1998] report that seasonal correlations can be as high as annual mean correlations, but different intercepts are to be expected in the regression and calibration of proxy data and instrumental temperatures.

An approach that has been successfully applied to capture potential seasonal biases in alkenone data is the *production-weighted temperature* [*Sonzogni et al.*, 1997; *Müller et al.*, 1998; *Schneider et al.*, 2010]. Using satellite-derived primary production rates and assuming a high correlation between coccolithophorid production and total primary production, the covariance between temperatures and primary production can be exploited to develop a seasonal weighting of the alkenone data. This method has enabled a better understanding of the discrepancies between alkenone and Mg/Ca-derived Holocene temperature trends in terms of seasonality and orbital-scale forcings.

Inspired by the sediment trap studies discussed above, but also recognizing the potential caveats of these sparse data sets, we propose the possibility that on average $U^{k'}_{37}$-derived SSTs in late Pleistocene sediments from the equatorial Pacific may be biased toward the winter season. While this is certainly not universally true, we will adopt this idea as a working hypothesis to further test whether it may help to explain diverging trends of alkenone-based SST and Mg/Ca-based SST reconstructions. In our study we further make the commonly applied assumption that the oceanographic and ecological processes that promote these depth and seasonal growth patterns have remained roughly constant throughout at least the last 21 ka so that sedimentary alkenones from the Last Glacial Maximum (LGM) were likely to have been produced in the surface mixed layer in boreal winter. We discuss the possibility for changes of this seasonal relationship in section 3.

2.5. Orbital-Scale Variations in *G. ruber* Mg/Ca-Based SSTs in the Equatorial Pacific

While $U^{k'}_{37}$-based SSTs increased across the equatorial Pacific through the Holocene, SSTs derived from Mg/Ca ratios in the planktonic foraminifera *G. ruber* decreased. Throughout the WEP (composite index in Figure 1, top left) and EEP (composite index in Figure 1, top right) *G. ruber* Mg/Ca SST records exhibit a considerable Holocene cooling of 0.5–1.5°C, starting around 9 ka B.P. There is also a clear indication for an earlier onset of deglacial warming, in particular in the EEP, compared to the alkenone record. The Mg/Ca SSTs also exhibit a stronger precessional signal in the sense that maximum SSTs are attained around 9 ka and minimum SSTs around 20 ka B.P. The discrepancies with the alkenone data, namely, during the Holocene, are striking and call for an explanation.

Holocene Mg/Ca trends could in principle also be generated by trends in calcium carbonate dissolution [*Regenberg et al.*, 2014]. However, the high diversity of depositional settings and water depths in 10 cores, exhibiting the Holocene Mg/Ca trends (Figure 1, top) renders it highly unlikely that dissolution is the main cause [*Brown and Elderfield*, 1996; *Lea et al.*, 2000; *Rosenthal and Lohmann*, 2002; *Rosenthal et al.*, 2000]. The one exception would be if equatorial Pacific waters from 1 to 4 km became more corrosive to $CaCO_3$ during the Holocene, such would occur if the carbonate ion concentration of the entire tropical Pacific Ocean below 1 km gradually and continuously decreased. Such a scenario cannot be ruled out entirely because a substan-

tial decrease in the carbonate ion concentration of the deep (>3 km) equatorial Pacific has been inferred from planktonic foraminiferal shell weights since the LGM [*Broecker and Clark*, 2001] with an estimated 8 mol/kg decline in [CO_3^{2-}] occurring in the Holocene at depths below 3 km [*Broecker et al.*, 1999]. In the 1–3 km depth range, however, these studies report no evidence for a carbonate ion decline of this magnitude during the Holocene. Barring a dissolution-derived cooling artifact, the Holocene cooling trend implied by *G. ruber* Mg/Ca is assumed real and could be explained by (i) a decrease in the mean annual temperature of surface waters throughout the equatorial Pacific, (ii) cooling during the season that *G. ruber* grows, (iii) a gradual deepening of the depth habitat of *G. ruber*, or (iv) the growing season of *G. ruber* became increasingly the cold season throughout the Holocene at the expense of the warm season. This latter explanation would complicate the interpretation of Mg/Ca-derived temperature tremendously.

To further explore possibility (ii), we briefly review recent sediment trap studies. The depth habitat of *G. ruber* is generally assumed to be the euphotic zone since it is host to photo-autotrophic symbionts. This is borne out by net tow studies in the western equatorial Pacific [*Lin and Hsieh*, 2007] and the eastern equatorial Pacific [*Fairbanks et al.*, 1982]. The season of maximum *G. ruber* abundance in the western equatorial Pacific is boreal summer [*Kawahata et al.*, 2002; *Lin et al.*, 2004; *Tian et al.*, 2005; *Troelstra and Kroon*, 1989; *Wiesner et al.*, 1996]. *G. ruber* also reach maximum abundances in boreal summer in the eastern tropical Pacific, as indicated by the sediment trap study by *Thunell and Reynolds* [1984] using data from the Panama Basin (Figure 4, bottom). In the Baja California region *G. ruber* abundances in the stratified surface mixed layer also tend to peak during the summer/fall [*McConnell and Thunell*, 2005; *Wejnert et al.*, 2010]. Whereas there may be site-specific regional differences, with respect to when exactly *G. ruber* abundances peak, we infer that there appears to be a general tendency for a *G. ruber* summer maximum in the tropical Pacific. This would translate also into a summer bias of calcification temperatures.

2.6. Discussion of Seasonal Sensitivities in Proxy Data

Our analysis above has critically assessed various lines of reasoning to suggest that EEP/WEP alkenone and Mg/Ca SST reconstructions could be seasonally biased. However, the exact determination of the seasonal biases for our proxy locations (Figure 2) remains inconclusive. For instance, spatial inhomogeneities in the seasonal production of phytoplankton (Figure 2) can complicate the situation. Furthermore, with only very few long-term tropical Pacific sediment trap records available (Figure 4), it is very difficult to translate their results to other regions in the equatorial Pacific. Another conundrum arises from the fact that EEP alkenone core-top data show a relatively weak correlation (Figure 3) with boreal winter SST, in spite of recent findings from tropical oceans suggesting potential boreal winter biases in the production of alkenone-producing coccolithophores.

Given these uncertainties, it becomes apparent that a different approach is needed to reconcile the diverging trends in alkenone and Mg/Ca-based SSTs in the EEP and WEP (Figure 1). Rather than relying on sparse observational present-day data sets, we will exploit the physical climate responses to the well-known external forcings during the last 21 ka using a three-dimensional climate model. By comparing the spatially averaged paleo-SST reconstructions in Figure 1 with simulated seasonal temperatures and by focusing on the onset of seasonally modulated deglacial warming and Holocene trends, we will be able to deduce potential seasonal biases in the EEP and WEP alkenone and Mg/Ca SST data sets.

3. Model-Proxy Data Comparisons Over the Last 21 ka

Next, we use a model of intermediate complexity to evaluate the hypothesis that the differing trends in SST derived from alkenones and Mg/Ca can be attributed to insolation-driven changes in the summer and winter seasons in the equatorial Pacific. Previous studies have focused on Holocene temperature trends and used time slice experiments conducted with Coupled General Circulation Models [*Schneider et al.*, 2010] or transient coupled model simulations forced only by orbital insolation variations [*Lorenz et al.*, 2006; *Lohmann et al.*, 2013]. To estimate the effect of time-varying greenhouse gases, ice sheets, and orbital insolation variations on the surface temperature evolution in the equatorial Pacific, we use the earth system model of intermediate complexity Loch–VECODE– ECBilt–CLIO–Agism Model (LOVECLIM) in a series of transient climate simulations covering the last 21 ka.

3.1. Model Description

The atmospheric component of the coupled model LOVECLIM is EMIC Climate deBilt (ECBilt) [*Opsteegh et al.*, 1998], a spectral T21, three-level model, based on quasi-geostrophic equations extended by estimates

of the neglected ageostrophic terms in order to close the equations at the equator. The model contains a full hydrological cycle which is closed over land by a bucket model for soil moisture. Synoptic variability associated with weather patterns is explicitly computed. Diabatic heating due to radiative fluxes, the release of latent heat, and the exchange of sensible heat with the surface are parameterized and a prescribed present-day cloud climatology is used. The sea ice-ocean component of LOVECLIM, Coupled Large-Scale Ice–Ocean (Clio) [*Goosse et al.*, 1999; *Goosse and Fichefet*, 1999; *Campin and Goosse*, 1999] consists of a free-surface primitive equation model with 3°×3° resolution coupled to a thermodynamic-dynamic sea ice model.

Coupling between atmosphere and ocean is done via freshwater and heat fluxes rather than by virtual salt fluxes. To avoid a singularity at the North Pole, the oceanic component makes use of two subgrids: The first one is based on classic longitude and latitude coordinates and covers the whole ocean except the North Atlantic and Arctic ocean. These are covered by the second spherical subgrid, which is rotated and has its poles at the equator in the Pacific (111° West) and Indian Ocean (69° East). The coupled model also uses a very weak freshwater flux correction, which represents a moisture transport from the North Atlantic to the North Pacific. For our purposes here the effect of this freshwater flux correction can be neglected.

This LOVECLIM model and its former version ECBilt-Clio have been used extensively in previous transient paleoclimate modeling studies [e.g., *Renssen et al.*, 2005; *Goosse et al.*, 2006; *Timm and Timmermann*, 2007; *Timm et al.*, 2007; *Timmermann et al.*, 2009; *Timm et al.*, 2010; *Menviel et al.*, 2011].

3.2. External Forcing

To quantify the effects of orbital forcing and other time-varying boundary conditions on the evolution of seasonal temperatures, we present the solutions from three transient model experiments. Experiment *TR-21* (described in *Timm and Timmermann* [2007]) uses time-varying atmospheric CO_2, CH_4, and N_2O concentrations for the last 21 ka, following greenhouse gas measurements from the European Project for Ice Coring in Antarctica DOME C ice core [*Spahni et al.*, 2005; *Lüthi et al.*, 2008]. Orbitally induced variations in the daily mean irradiance are calculated following *Berger* [1978]. The ice sheet forcing in this experiment uses 1000 yearlong slabs provided by the *Peltier* [1994] paleotopography reconstructions. The effect of ice sheets is felt by the atmosphere through changes in topography, albedo, and changing vegetation coverage. This experiment does not employ orbital acceleration [see *Timm and Timmermann*, 2007] and it was initialized from an equilibrated coupled Last Glacial Maximum (LGM) simulation.

Experiment *ORB* (described in *Timmermann et al.* [2009]) only uses time-varying orbital forcing, keeping greenhouse gas and ice sheet forcing at LGM values. This model simulation that started from an equilibrated LGM state was accelerated by a factor of 10 to save computing time. Hence, the 21 ka forcing history is compressed into a 2100 yearlong simulation. As demonstrated in *Timm and Timmermann* [2007], an acceleration factor of 10 is not expected to influence equatorial SST dynamics greatly. This experiment will provide an estimate of the effects of orbital forcing only on equatorial SST during the last 21 ka.

We also analyzed a three-member ensemble of transient orbitally forced simulations conducted with the ECHO-G coupled general circulation model. More details on this experiment can be found in *Lorenz and Lohmann* [2004], *Felis et al.* [2004], *Lorenz et al.* [2006], *Timmermann et al.* [2007], and *Uchikawa et al.* [2010]. Under preindustrial CO_2 concentrations, the *ECHO-G* experiment uses accelerated orbital forcing and an acceleration factor of 100. The model starts with the orbital configuration corresponding to the year 142 ka B.P. and ends in the year 22.9 ka after present. We calculated the mean of the simulated seasonal temperatures averaged over three-ensemble members and focus only on the period 21 ka B.P. to 0 ka B.P. From the LOVECLIM and ECHO-G experiments we extracted fixed-length seasonal mean surface temperatures area averaged over the northeastern (6°S–6°N and 260–280°E) and northwestern equatorial Pacific (10°S–10°N and 105–160°E).

3.3. Model-Paleoproxy Data Comparison and Inferences on Seasonal Biases

Figure 6 shows the simulated late boreal summer (July, August, and September mean) and winter (December, January, and February mean) temperatures in the eastern and western equatorial Pacific from *TR-21*, in comparison with the stacked Mg/Ca and alkenone SST records from Figure 1. Both seasons were chosen to yield an optimal match between model simulation and proxy data. We observe a good qualitative match between model and proxy data. In both the western and eastern equatorial Pacific there is a tendency for the simulated temperatures to peak around 10 ka, with a slowly decreasing trend into the late

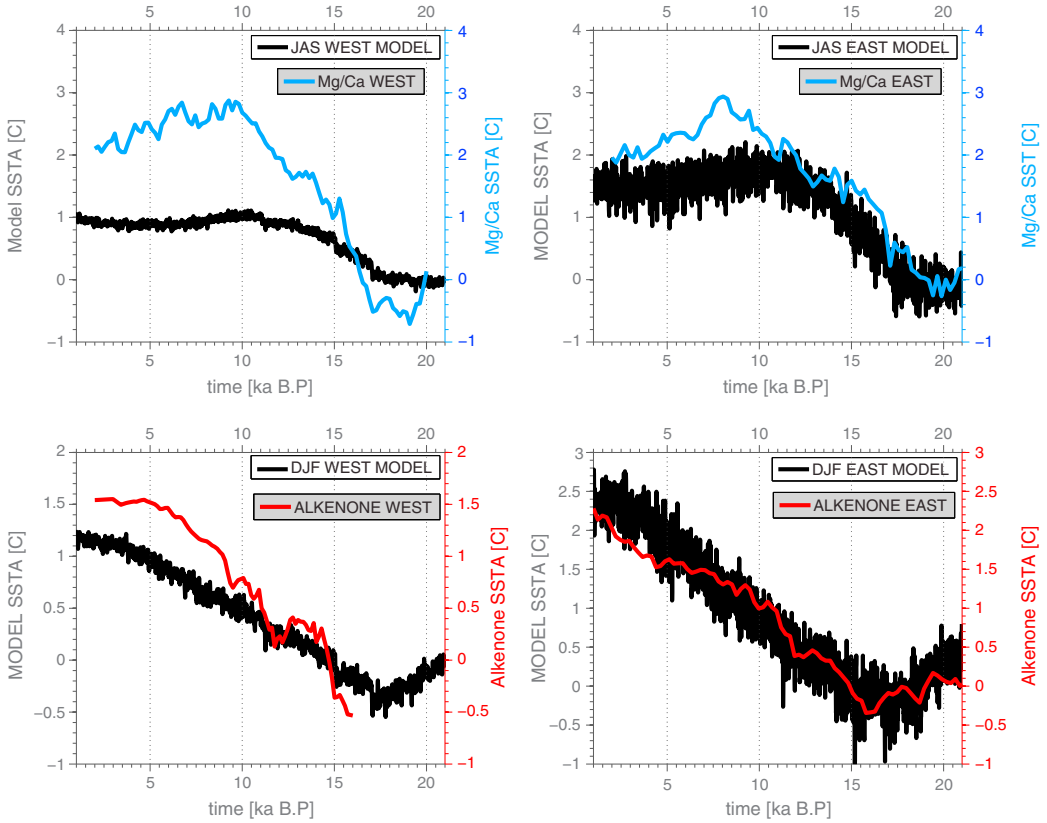

Figure 6. (top left) Composite of Mg/Ca-based SST reconstructions (blue) from the western equatorial Pacific and simulated July/August/September (JAS) (black) surface temperatures in the western equatorial Pacific, averaged from 10°S–10°N to 105–160°E (see Figure 2 for region). Note the different abscissa scales for model and proxy data. (top right) Same as top left but for the model area 6°S–6°N and 260–280°E (see Figure 2 for region) and using the eastern equatorial Pacific Mg/Ca composite from Figure 1, top right. (bottom left) Composite of alkenone SST reconstructions (red) from the western equatorial Pacific and simulated December/January/February (DJF) (black) surface temperatures in the western equatorial Pacific, averaged from 10°S–10°N to 105–160°E. (bottom right) Same as bottom left but for the model area 6°S–6°N and 260–280°E and using the eastern equatorial Pacific alkenone composite from Figure 1, bottom right.

Holocene. It is only during summer and fall that a decreasing temperature trend during the Holocene is simulated in *TR-21* (Figure 6). The onset of the deglacial warming is well captured by the simulated summer temperatures, although the model simulations do not invoke millennial-scale forcings such as freshwater pulses related to Heinrich event 1 and the Younger Dryas. It is important to note the amplitude of the simulated deglacial July/August/September (JAS) temperature trends is underestimated by a factor of 2–3 compared to the Mg/Ca SST reconstructions. This is likely due to the fact that LOVECLIM exhibits a relatively strong atmospheric damping to equatorial SST anomalies. The simulated December/January/February (DJF) temperatures in the eastern and western equatorial Pacific track the continuous reconstructed alkenone temperature trend throughout the Holocene as well as the onset of the deglacial warming around 16 ka B.P. In the western equatorial Pacific the simulated amplitude of the overall warming trend is underestimated, whereas it is well reproduced in the eastern equatorial Pacific. These results suggest that a seasonal interpretation of Mg/Ca and alkenone data may help reconciling their divergent behavior during the Holocene and the last glacial termination.

To further disentangle the seasonal climate evolution in the eastern equatorial Pacific in terms of orbital and other forcings, we study the simulated temperature history in experiment *ORB* (Figure 7). The DJF temperature evolution exhibits a precession signal, which contributes by about 1°C to the Holocene trend, seen in the alkenone proxy data. The temperature trend in DJF in *TR-21* is governed to first order by the CO_2 forced signal, and the orbital effect with some contributions from the decreasing Laurentide ice sheet height on equatorial Pacific SST, as discussed in *Timmermann et al.* [2004] using an earlier version of LOVECLIM. The origin of delayed deglacial DJF warming starting around 16 ka B.P. can be traced back to the fact that dur-

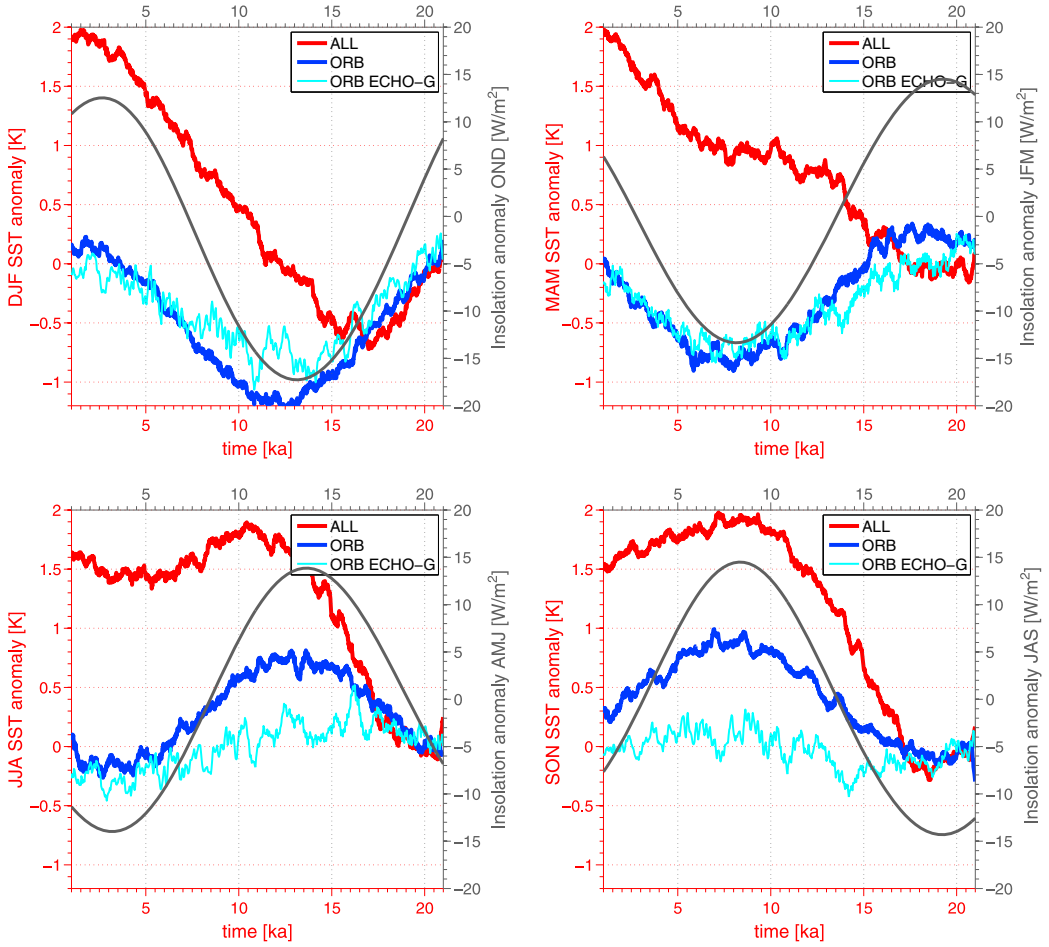

Figure 7. (top left) Simulated DJF temperature anomalies in the eastern equatorial Pacific (average from 6°S–6°N to 260–280°E, see Figure 2 for region) for the transient simulations that uses all forcings (red) *TR-21* and a transient run that uses only orbital forcing *ORB* (blue), whereas greenhouse gas and ice sheet forcings are kept fixed at LGM values. The dark grey line represents the near-equatorial orbital forcing anomalies 2 months prior to DJF. (top right) The same as top left but for MAM. (bottom left) The same as top left but for JJA. (bottom right) The same as bottom left but for SON. Note the 2–3 month delay between orbital forcing and the temperature response in *ORB*. The cyan lines represent the respective three-member ensemble mean seasonal data of eastern equatorial Pacific SST, as simulated by the orbitally forced transient *ECHO-G* experiment [see *Lorenz et al.*, 2006; *Timmermann et al.*, 2007].

ing the period 20–16 ka B.P. the CO_2 and ice sheet forcings are still relatively weak, and the temperature evolution is largely controlled by the orbitally induced cooling trend.

Note also that, in contrast to the considerations of *Leduc et al.* [2010], the DJF insolation signal is not in phase with the DJF temperature evolution (see Figure 7, dark grey lines). This can be explained by the fact that the mixed layer temperature evolution due to orbitally induced changes of the shortwave radiation is to first order governed by

$$T(t) = \int_0^t \frac{Q_{\mathrm{inc}}(t)(1-\overline{\alpha})}{c_p \rho H_{\mathrm{mix}}}\, e^{-\lambda(t-t')}\, \mathrm{d}t', \tag{1}$$

where $\overline{\alpha}$ corresponds to the long-term mean regional albedo in the eastern equatorial Pacific (cloud-albedo feedbacks are ignored for simplicity) and $Q_{\mathrm{inc}}(t)$ denotes the orbitally induced variations in top-of-the atmosphere solar insolation (i.e., the orbitally modulated annual cycle forcing). The heat capacity of water is c_p and ρ the density of seawater. The average mixed layer depth is denoted as H_{mix}. The damping rate λ partly controls the delay between forcing and response. In the eastern equatorial Pacific with a mean mixed layer depth of $H_{\mathrm{mix}} = 30$ m and $\lambda^{-1} \sim$3–4 months [*Barnett et al.*, 1991], the annual cycle forcing $Q(t)$ and its modulation through the Milankovitch cycles translates into a temperature response that lags the forcing

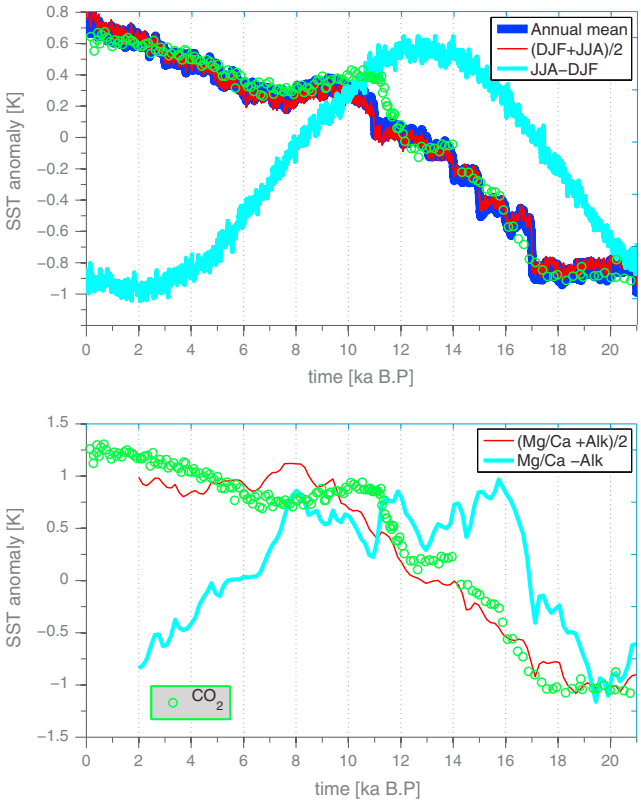

Figure 8. (top) Simulated eastern equatorial Pacific annual mean (average from 6°S–6°N and 260–280°E, see Figure 2 for region) (blue line, behind red line) SST anomalies, atmospheric CO_2 concentrations (green circles) from *Lüthi et al.* [2008] and average of boreal summer and winter SST (red line, a proxy for the annual mean) and boreal summer minus winter temperatures (cyan line, a proxy for the strength of the seasonal cycle). These data are obtained from the *TR-21* simulation. (bottom) Averaged Mg/Ca and alkenone-based SST anomaly composite (using composites from Figure 1) for the eastern equatorial Pacific (red), atmospheric CO_2 concentrations (blue circles), and Mg/Ca minus alkenone temperature composites (cyan).

by about 2 months [*Laepple and Lohmann*, 2009]. In other words the DJF (MAM, JJA, and SON) temperatures in *ORB* will be determined by OND (JFM, AMJ, and JAS) seasonal insolation changes associated with the precessional cycle.

The March/April/May (MAM) SST trend in *ORB* (Figure 7, top right) features a precessional-scale cooling from 20–8 ka B.P. and a subsequent warming that contributes to the middle-to-late Holocene warming induced by the other time-varying boundary conditions, namely, the orbital insolation changes during January/February/March (JFM). The boreal summer season June/July/August (JJA) (Figure 7, bottom left) is marked by a temperature maximum around 11–12 ka B.P. and a subsequent cooling trend that continues until 5 ka B.P. The JJA SST variations in *ORB* are a result of the seasonally averaged insolation variations during April/May/June (AMJ). An early warming occurs during JJA as a result of increasing insolation during AMJ. Clearly, the seasonal interpretation of the alkenone and Mg/Ca SSTs, capturing different phases of the precessional cycle, can help to explain the different onsets in deglacial warming in Figure 1. The September/October/November (SON) boreal fall temperature evolution in *TR-21* is a combination of greenhouse gas, ice sheet forcing, and a precessional cycle that peaks around 9 ka B.P. According to equation (1) and assuming a damping time scale λ^{-1} of 2–3 months, we conclude that the late summer orbital forcing is mainly responsible for the SON temperature variations.

Comparison of the simulated northeastern equatorial Pacific SSTs in *ORB* with an orbitally forced run (Figure 6, cyan lines) that was performed with the *ECHO-G* coupled general circulation model [*Lorenz and Lohmann*, 2004; *Felis et al.*, 2004; *Lorenz et al.*, 2006; *Timmermann et al.*, 2007; *Uchikawa et al.*, 2010] suggests that the tropical SST sensitivity to orbital forcing is similar in LOVECLIM to the more realistic ECHO-G model.

These idealized modeling results suggest that the seasonal SST evolution in the equatorial Pacific can be interpreted as a lagged response to the seasonally varying orbital forcing anomalies, greenhouse gas variations, and ice sheet forcing. The response of equatorial SSTs to just greenhouse gas and the ice sheet forcing is relatively constant throughout the year (not shown). Hence, to explain the different behavior of $U^{k'}_{37}$-based and Mg/Ca-based SST, orbital forcing from different seasons has to be invoked.

3.4. Combining Seasonal Model and Proxy Data

Rather than discarding one SST proxy over another, our study suggests that they provide complementary information that can be further exploited to estimate annual mean temperatures, as well as the strength of the seasonal cycle in SST. This approach is demonstrated in Figure 8. In fact, using the transient climate model experiment *TR-21*, we can test how well the annual mean temperature variations in the EEP (Figure 8,

top, blue line, behind red line) can be reconstructed by just using the mean of boreal summer and boreal winter temperatures (Figure 8, top, red line). The resulting time series are virtually identical. Furthermore, we can calculate the difference between simulated boreal summer and boreal winter temperatures as a proxy for the strength of the seasonal cycle in SST. The resulting time series (Figure 8, top, cyan line) exhibits a clear precessional cycle with a maximum peaking around 12–13 ka B.P. and is virtually identical to the strength of the seasonal cycle (not shown). Inspired by these results and the proposed seasonal interpretation of Mg/Ca, $U^{k'}_{37}$ data, we calculate the average and difference of Mg/Ca SST anomalies and alkenone SST anomalies (Figure 8, bottom). The average SST of alkenone and SST is quite similar to the simulated annual mean temperature (Figure 8, top, blue line). The difference between Mg/Ca and alkenone-based SSTs (Figure 8, bottom, cyan line) shows similar characteristics to the model simulated annual cycle strength, except for a relatively long plateau between 14 and 10 ka B.P.

From this analysis, we observe that annual mean EEP SST variations, derived from the combination of alkenone and Mg/Ca SST composites appear to be strongly linked to the CO_2 radiative forcing. The overall glacial/amplitude attains values of up to 2°C, which is lower than estimates of annual mean SST differences (~3°C) from the WEP [*Tachikawa et al.*, 2014] (their Figure S1 based on cores MD05-2920, MD98-2161, ODP806 B, MD06-2067, MD01-2378, and MD97-2140). Together these results suggest a possible weakening of the zonal SST gradient for glacial conditions. Whether glacial/interglacial CO_2 changes were the controlling factor for this reduction is uncertain, given the presence of other potential contributors to EEP SST changes associated with, for instance, ice sheet-driven changes of the subtropical cells [*Timmermann et al.*, 2004].

4. Summary and Discussion

We have attempted to explain why alkenone and Mg/Ca-derived SST reconstructions in the equatorial Pacific often diverge from one another during the last 21 kyr. In particular, alkenone records across the equatorial Pacific indicate a warming trend during the Holocene, while Mg/Ca records indicate cooling. By using a model of intermediate complexity driven by insolation, greenhouse gases, and ice sheets, we are able to show that these divergent trends could be explained by differing seasons of growth, with alkenone production in the boreal winter and *G. ruber* production during boreal summer. This timing of growth is consistent with low-latitude Pacific sediment trap studies [*Brown and Yoder*, 1994; *Wiesner et al.*, 1996; *Chen et al.*, 2007; *Ziveri and Thunell*, 2000; *Harada et al.*, 2001]. However, these primarily model-based conclusions need to be interpreted with caution, given the spatial inhomogeneity of seasonal phytoplankton production rates discussed in section 2. Moreover, the inferred seasonal biases for spatially averaged eastern and western equatorial Pacific alkenone and Mg/Ca SST reconstructions are by no means universal and should not be applied to other regions.

Previous sediment trap studies suggest that on average *G. ruber* abundances in the tropical Pacific peak in boreal summer. Late summer temperatures (average of July, August, and September) simulated by a transient 21 ka simulation conducted with the LOVECLIM earth system model reproduce some key features of the Mg/Ca SST data compilation such as the Holocene cooling trend and the onset of deglacial warming around 17–18 ka B.P. Due to a 2 month lag between annual insolation and SSTs in the equatorial Pacific, we conclude that Mg/Ca SSTs, at least during the last 21 ka, were driven by early summer insolation changes, in combination with other forcings that act year round such as greenhouse gas forcing and the remote effect of the glacial ice sheets on the atmospheric circulation. Other factors that may contribute to the evolution of Mg/Ca temperatures include salinity variations [e.g., *Hertzberg and Schmidt*, 2013; *Hönisch et al.*, 2013] that were affected by changes in global ice volume as well as changes in the position of the Intertropical Convergence Zones. This aspect of the Mg/Ca-temperature calibrations has not been thoroughly discussed in our study but is likely to complicate the interpretation of Mg/Ca-based temperature signals in the tropical Pacific.

According to sediment trap data in the tropical Pacific [e.g., *Harada et al.*, 2001; *Chen et al.*, 2007], coccolithophorid blooms have the tendency to occur during boreal winter months. In fact, the simulated winter temperatures in the equatorial Pacific match the alkenone reconstructions qualitatively (and in the EEP also quantitatively) well. The increasing late fall to early winter insolation trend during the Holocene, in combination with increasing CO_2 concentrations, leads to a near-monotonic increase in alkenone temperatures. The somewhat delayed deglacial warming can be attributed to the fact that the late fall to early winter

insolation drops from the LGM into the early Holocene which compensates for some of the CO_2-induced winter temperature changes between 19 and 16 ka B.P. The effect of millennial-scale variability on the timing of deglacial temperature changes in the EEP is further discussed in *Dubois et al.* [2014]. A word of caution is necessary here. It should be noted that the although the model-derived boreal winter alkenone interpretation for the aggregated equatorial Pacific cores proposed here is consistent with several tropical Pacific sediment core studies [*Brown and Yoder*, 1994; *Wiesner et al.*, 1996; *Chen et al.*, 2007; *Ziveri and Thunell*, 2000; *Harada et al.*, 2001], it seems inconsistent with the results of our statistical EEP core-top analysis, which in fact identifies the months of February and March, as those with the lowest spatial correlation with the core-top data. Furthermore, we found high spatial heterogeneity in seasonal chlorophyll concentrations (Figure 2). If this was also true for the corresponding fluxes of coccolithophores this "patchiness" may further limit the application of our conclusions to individual sites.

While acknowledging some important model/proxy data mismatches, we propose that based on our model analysis, the most parsimonious explanation for divergent trends in equatorial Pacific SST inferred from alkenones and *G. ruber* Mg/Ca would be that alkenone producers and *G. ruber* live in different seasons in the tropical Pacific and that orbital precession-driven changes in insolation could help reconcile the divergent behavior of alkenone and Mg/Ca SSTs in the equatorial Pacific. This interpretation would offer the potential of combining $U^{k'}_{37}$ and Mg/Ca data of *G. ruber* from different cores to obtain information on seasonality *and* annual mean conditions. We recommend that future efforts to extract information on EEP climate from sediment cores should exploit this unique opportunity rather than focus just on one of the proxies.

Acknowledgments
The authors would like to thank Tom Koutavas, Guillaume Leduc, Nathalie Dubois, and Markus Kienast for providing their data sets from the tropical Pacific and for insightful discussions. We are also grateful to Stephan Lorenz for making the ECHO-G transient runs available to us. Support for this research came in part from grants NSF-OCE-0624954 (J.S.) and NOAA-NA06OAR4310122 (J.S.). A.T. acknowledges funding from NSF grant 1010869. Additional support was provided by the Japan Agency for Marine-Earth Science and Technology (JAMSTEC), through their sponsorship of research activities at the International Pacific Research Center. Data presented in this paper will be shared upon request.

References

Ashkenazy, Y., and E. Tziperman (2006), Scenarios regarding the lead of equatorial sea surface temperature over global ice volume, *Paleoceanography*, *21*, PA2006, doi:10.1029/2005PA001232.

Barnett, T., M. Latif, E. Kirk, and E. Roeckner (1991), On ENSO physics, *J. Clim.*, *4*, 487–515.

Bentaleb, I., M. Fontugne, and L. Beaufort (2002), Long-chain alkenones and $U^{k'}_{37}$ variability along a south-north transect in the Western Pacific Ocean, *Global Planet. Change*, *34*, 173–183.

Berger, A. L. (1978), Long-term variations of daily insolation and quaternary climatic changes, *J. Atmos. Sci.*, *35*(12), 2362–2367.

Broecker, W., and E. Clark (2001), Glacial-to-Holocene redistribution of carbonate ion in the deep sea, *Science*, *294*, 2152–2155.

Broecker, W., E. Clark, D. McCorkle, T.-H. Peng, I. Hajdas, and G. Bonani (1999), Evidence for a reduction in the carbonate ion content of the deep sea during the course of the Holocene, *Paleoceanography*, *14*, 744–752.

Brown, C., and J. Yoder (1994), Coccolithophorid blooms in the global ocean, *J. Geophys. Res.*, *99*(C4), 7467–7482.

Brown, S., and H. Elderfield (1996), Variations in Mg/Ca and Sr/Ca ratios of planktonic foraminifera caused by postdepositional dissolution: Evidence of shallow Mg-dependent dissolution, *Paleoceanography*, *11*, 543–551.

Campin, J., and H. Goosse (1999), A parameterization of dense overflow in large-scale ocean models in z coordinate, *Tellus A*, *51*, 412–430.

Chen, Y.-L., H.-Y. Chen, and C.-W. Chung (2007), Seasonal variability of coccolithophore abundance and assemblage in the northern South China Sea, *Deep Sea Res. Part II*, *54*(14–15), 1617–1633.

Cohen, J., and P. Cohen (1983), *Applied Multiple Regression/Correlation Analysis for the Behavioral Sciences*, Lawrence Erlbaum, Oxford, England.

Conte, M., M.-A. Sicre, C. Rühlemann, J. C. Weber, S. Schulte, D. Schulz-Bull, and T. Blanz (2006), Global temperatur calibration of the alkenone unsaturation indx $U^{K'}_{37}$ in surface waters and comparison with surface sediments, *Geochem. Geophys. Geosyst.*, *7*, Q2005, doi:10.1029/2005GC001054.

de Garidel-Thoron, T., Y. Rosenthal, L. Beaufort, E. Bard, C. Sonzogni, and A. Mix (2007), A multiproxy assessment of the western equatorial Pacific hydrography during the last 30 kyr, *Paleoceanography*, *22*, PA3204, doi:10.1029/2006PA001269.

Dubois, N., M. Kienast, S. Kienast, and A. Timmermann (2014), Millennial-scale Atlantic/East Pacific sea surface temperature linkages during the last 100,000 years, *Earth Planet. Sci. Lett.*, *396*, 134–142.

Fairbanks, R., M. Sverdlove, R. Free, P. Wiebe, and A. Be (1982), Vertical distribution and isotopic fractionation of living planktonic foraminifera from the Panama Basin, *Nature*, *298*, 841–844.

Felis, T., G. Lohmann, H. Kuhnert, S. Lorenz, D. Scholz, J. Pätzold, A. A. Rousan, and S. Al-Moghrabi (2004), Increased seasonality in Middle East temperatures during the last interglacial period, *Nature*, *429*, 164–168.

Fraile, O., M. Schulz, S. Mulitza, U. Merkel, M. Prange, and A. Paul (2009), Modeling the seasonal distribution of planktonic foraminifera during the last glacial maximum, *Paleoceanography*, *24*, PA2216, doi:10.1029/2008PA001686.

Goosse, H., O. Arzel, J. Luterbacher, M. E. Mann, H. Renssen, N. Riedwyl, A. Timmermann, E. Xoplaki, and H. Wanner (2006), The origin of the "European Medieval Warm Period", *Clim. Past*, *2*, 99–113.

Goosse, H., E. Deleersnijder, T. Fichefet, and M. England (1999), Sensitivity of a global coupled ocean-sea ice model to the parameterization of vertical mixing, *J. Geophys. Res*, *104*(C6), 13,681–13,695.

Goosse, H., and T. Fichefet (1999), Importance of ice-ocean interactions for the global ocean circulation: A model study, *J. Geophys. Res*, *104*(C10), 23,337–23,355.

Harada, N., N. Handa, K. Harada, and H. Matsuoka (2001), Alkenones and particulate fluxes in sediment traps from the central equatorial Pacific, *Deep Sea Res. Part I*, *48*, 891–907.

Harada, N., et al. (2012), Sea surface and subsurface temperature changes in the Okhotsk Sea and adjacent North Pacific during the last glacial maximum and deglaciation, *Deep Sea Res. Part II*, *61–64*, 93–105.

Hernández-Becerril, D., E. BravoSierra, and J. Aké-Castillo (2007), Phytoplankton on the western coasts of Baja California in two different seasons in 1998, *Sci. Mar.*, *71*, 735–743, doi:10.3989/scimar.2007.71n4735.

Hertzberg, J. E., and M. W. Schmidt (2013), Refining Globigerinoides ruber Mg/Ca paleothermometry in the Atlantic Ocean, *Earth Planet. Sci. Lett.*, *383*, 123–133.

Hönisch, B., K. A. Allen, D. W. Lea, H. J. Spero, S. M. Eggin, J. Arbuszewski, P. deMenocal, Y. Rosenthal, A. D. Russell, and H. Elderfield (2013), The influence of salinity on Mg/Ca in planktic foraminifers—Evidence from cultures, core-top sediments and complementary $\delta^{18}O$, *Geochim. Cosmochim. Acta*, *121*, 196–213.

Kawahata, H., A. Nishimura, and M. Gagan (2002), Seasonal change in foraminiferal production in the western equatorial Pacific warm pool: Evidence from sediment trap experiments, *Deep Sea Res. Part II*, *49*(13–14), 2783–2800.

Kienast, M., G. MacIntyre, N. Dubois, S. Higginson, C. Normandeau, C. Chazen, and T. D. Herbert (2012), Alkenone unsaturation in surface sediments from the eastern equatorial Pacific: Implications for SST reconstructions, *Paleoceanography*, *27*, PA1210, doi:10.1029/2011PA002254.

Kienast, M., S. Steinke, K. Stattegger, and S. Calvert (2001), Synchronous tropical South China Sea sst change and Greenland warming during deglaciation, *Science*, *291*, 2132–2134.

Kienast, S., M. Kienast, S. Jaccard, E. Calvert, and R. Francois (2006), Testing the silica leakage hypothesis with sedimentary opal records from the eastern equatorial Pacific over the last 150 kyrs, *Geophys. Res. Lett.*, *33*, L15607, doi:10.1029/2006GL026651.

Koutavas, A., and J. Sachs (2008), Northern timing of deglaciation in the eastern equatorial Pacific from alkenone paleothermometry, *Paleoceanography*, *23*, PA4205, doi:10.1029/2008PA001593.

Laepple, T., and G. Lohmann (2009), The seasonal cycle as template for climate variability on astronomical time scales, *Paleoceanography*, *24*, PA4201, doi:10.1029/2008PA001674.

Lea, D., D. Pak, C. Belanger, H. Spero, M. Hall, and N. Shackleton (2006), Paleoclimate history of galapagos surface waters over the last 135,000 yrs, *Quat. Sci. Rev.*, *25*, 1152–1167.

Lea, D., D. Pak, and H. Spero (2000), Climate impact of late quaternary equatorial Pacific sea surface temperature variations, *Science*, *289*, 1719–1724.

Leduc, G., R. Schneider, J. H. Kim, and G. Lohmann (2010), Holocene and Eemian sea surface temperature trends as revealed by alkenone and Mg/Ca paleothermometry, *Quat. Sci. Rev.*, *29*, 989–1004.

Leduc, G., L. Vidal, K. Tachikawa, F. Rostek, C. Sonzogni, L. Beaufort, and E. Bard (2007), Moisture transport across Central America as a positive feedback on abrupt climatic changes, *Nature*, *445*(7130), 908–911.

Lin, H., and H.-Y. Hsieh (2007), Seasonal variations of modern planktonic foraminifera in the South China Sea, *Deep Sea Res. Part II*, *54*(14–15), 1634–1644.

Lin, H., W.-C. Wang, and G.-W. Hung (2004), Seasonal variation of planktonic foraminiferal isotopic composition from sediment traps in the South China Sea, *Mar. Micropaleontol.*, *53*(3–4), 447–460.

Linsley, B., and Y. Rosenthal (2010), Holocene evolution of the indonesian throughflow and the western Pacific warm pool, *Nat. Geosci.*, *3*, 578–583.

Lohmann, G., M. Pfeiffer, T. Laepple, G. Leduc, and J.-H Kim (2013), A model-data comparison of the Holocene global sea surface temperature evolution, *Clim. Past*, *9*, 1807–1839, doi:10.5194/cp-9-1807-2013.

Lorenz, S., J.-H. Kim, N. Rimbu, R. Schneider, and G. Lohmann (2006), Orbitally driven insolation forcing on Holocene climate trends: Evidence from alkenone data and climate modeling, *Paleoceangraphy*, *21*, PA1002, doi:10.1029/2005PA001152.

Lorenz, S., and G. Lohmann (2004), Acceleration technique for Milankovitch type forcing in a coupled atmosphere-ocean circulation model: Method and application for the Holocene, *Clim. Dyn.*, *23*, 727–743, doi:10.1007/s00382-004-0469.

Lüthi, D., et al. (2008), High-resolution carbon dioxide concentration record 650,000–800,000 years before present, *Nature*, *453*, 379–382.

Martinez, I., D. Rincon, Y. Yokoyama, and T. Barrows (2006), Foraminifera and coccolithophorid assemblage changes in the Panama Basin during the last deglaciation: Response to sea-surface productivity induced by a transient climate change, *Palaeogeogr. Palaeoclimatol. Palaeoecol.*, *234*(1), 114–126.

McClain, C., M. Cleave, G. Feldman, W. Gregg, S. Hooker, and N. Kuring (1998), Science quality SeaWiFS data for global biosphere research, *Sea Technol.*, *39*, 10–16.

McConnell, M., and R. Thunell (2005), Calibration of the planktonic foraminiferal Mg/Ca paleothermometer: Sediment traps results from the Guaymas Basin, *Paleoceanography*, *20*, PA2016, doi:10.1029/2004PA001077.

Medina-Elizalde, M., and D. Lea (2005), The mid-pleistocene transition in the tropical Pacific, *Science*, *310*, 1009–1012.

Menviel, L., A. Timmermann, O. E. Timm, and A. Mouchet (2011), Deconstructing the Last Glacial termination: The role of millennial and orbital-scale forcings, *Quat. Sci. Rev.*, *30*, 1155–1172.

Monnin, E., A. Indermühle, A. Dällenbach, J. Flückiger, B. Stauffer, T. F. Stocker, D. Raynaud, and J.-M. Barnola (2001), Atmospheric CO_2 concentrations over the last glacial termination, *Science*, *291*, 112–114.

Müller, P., G. Kirst, G. Ruhland, I. von Storch, and A. Rosell-Melé (1998), Calibration of the alkenone paleotemperature index $U^{K'}_{37}$ based on core-tops from the eastern South Atlantic and the global ocean (60°n-60°s), *Geochim. Cosmochim. Acta*, *62*, 1757–1772.

Nürnberg, D., A. Müller, and R. R. Schneider (2000), Paleo-sea surface temperature calculations in the equatorial East Atlantic from Mg/Ca ratios in planktic foraminifera: A comparison to sea surface temperature estimates from $U^{K'}_{37}$, oxygen isotopes, and foraminiferal transfer function, *Paleoceanography*, *15*, 124–134.

Ohkouchi, N., K. Kawamura, H. Kawahata, and H. Okada (1999), Depth ranges of alkenone production in the central Pacific Ocean, *Global Biogeochem. Cycles*, *13*, 695–704.

Okada, H., and S. Honjo (1973), The distribution of ocanic coccolithophorids in the Pacific, *Deep Sea Res.*, *20*, 355–374.

Opsteegh, J., R. Haarsma, F. Selten, and A. Kattenberg (1998), ECBILT: A dynamic alternative to mixed boundary conditions in ocean models, *Tellus A*, *50*, 348–367.

Pahnke, K., J. Sachs, L. Keigwin, A. Timmermann, and S.-P. Xie (2007), Eastern tropical Pacific hydrologic changes during the past 27,000 years from d/h ratios in alkenones, *Paleoceanography*, *22*, PA4214, doi:10.1029/2007PA001468.

Peltier, W. R. (1994), Ice age paleotopography, *Science*, *265*, 195–201.

Pena, L., I. Cacho, P. Ferretti, and M. Hall (2008), El ninõ–Southern oscillation-like variability during glacial terminations and interlatitudinal teleconnections, *Paleoceanography*, *23*, PA3101, doi:10.1029/2008PA001620.

Regenberg, M., A. Regenberg, A. Garbe-Schönberg, and D. W. Lea (2014), Global dissolution effects on planktonic foraminiferal Mg/Ca ratios controlled by the calcite-saturation state of bottom waters, *Paleoceanography*, *29*, 127–142, doi:10.1002/2013PA002492.

Renssen, H., H. Goosse, and T. Fichefet (2005), Contrasting trends in North Atlantic deep-water formation in the Labrador Sea and Nordic Seas during the Holocene, *Geophys. Res. Lett*, *32*, L08711, doi:10.1029/2005GL022462.

Reynolds, R., N. Rayner, T. Smith, D. Stokes, and W. Wang (2002), An improved in situ and satellite SST analysis for climate, *J. Clim.*, *15*, 1609–1625.

Reynolds, R., T. Smith, C. Liu, D. B. Chelton, K. S. Casey, and M. G. Schlax (2007), Daily high-resolution-blended analyses for sea surface temperature, *J. Clim.*, *20*, 5473–5496.

Rosell-Melé, A., E. Bard, B. Grieger, C. Hewitt, P. Müller, and R. Schneider (2004), Sea surface temperature anomalies in the oceans at the LGM estimated from the alkenone-UK'_{37} index: Comparison with GCMs, *Geophys. Res. Lett*, *39*, L03208, doi:10.1029/2003GL018151.
Rosell-Melé, A., and F. G. Prahl (2013), Seasonality of UK'37 temperature estimates as inferred from sediment trap data, *Quat. Sci. Rev.*, *72*, 128–136, doi:10.1016/j.quascirev.2013.04.017.
Rosenthal, Y., and G. Lohmann (2002), Accurate estimation of sea surface temperatures using dissolution-corrected calibrations for Mg/Ca paleothermometry, *Paleoceanography*, *17*, 1044, doi:10.1029/2001PA000749, 3.
Rosenthal, Y., G. Lohmann, K. Lohmann, and R. Sherrell (2000), Incorporation and preservation of Mg in Globigerinoides sacculifer: Implications for reconstructing the temperature and 18O/16O of seawater, *Paleoceanography*, *15*(1), 135–145.
Schneider, B., G. Leduc, and W. Park (2010), Disentangling seasonal signals in Holocene climate trends by satellite-proxy integration, *Paleoceanography*, *25*, PA4217, doi:10.1029/2009PA001893.
Silverberg, N., A. Martinez, S. Aguíñiga, J. Carriquiry, N. Romero, E. Shumilin, and S. Cota (2004), Contrasts in sedimentation flux below the Southern California current in late 1996 and during the El Nino event of 1997–1998, *Estuarine Coastal Shelf Sci.*, *59*, 575–587.
Sonzogni, C., E. Bard, F. Rostek, R. Lafont, A. Rosell-Melé, and G. Eglinton (1997), Core-top calibration of the alkenone index vs sea surface temperature in the Indian Ocean, *Deep Sea Res. Part II*, *44*, 1445–1460.
Spahni, R., et al. (2005), Atmospheric methane and nitrous oxide of the late Pleistocene from Antarctic ice cores, *Science*, *310*, 1317–1321.
Stein, K., A. Timmermann, and N. Schneider (2011), Phase synchronization of the El Niño-Southern Oscillation with the annual cycle, *Phys. Rev. Lett.*, *107*(12), 128,501.
Steinke, S., M. Kienast, J. Groeneveld, L.-C. Lin, M.-T. Chen, and R. Rendle-Buehring (2008), Proxy dependence of the temporal pattern of deglacial warming in the tropical south china sea: Toward resolving seasonality, *Quat. Sci. Rev.*, *27*, 688–700.
Stott, L., K. Cannariato, R. Thunell, G. H. Haug, A. Koutavas, and S. Lund (2004), Decline of sea surface temperature and salinity in the western tropical Pacific Ocean during the Holocene epoch, *Nature*, *431*, 56–59.
Stott, L., A. Timmermann, and R. Thunell (2007), Southern Hemisphere and deep-sea warming led deglacial atmospheric CO_2 rise and tropical warming, *Science*, *318*, 435–438.
Tachikawa, K., A. Timmermann, L. Vidal, C. Sonzogni, and O. Elison Timm (2014), CO_2 radiative forcing and intertropical convergence zone influences on western Pacific warm pool climate over the past 400 ka, *Quat. Sci. Rev.*, *86*(15), 24–34.
Thunell, R., and L. Reynolds (1984), Sedimentation of planktonic foraminifera: Seasonal changes in species flux in the Panama Basin, *Micropaleontology*, *30*(3), 243–262.
Tian, J., P. Wang, R. Chen, and X. Cheng (2005), Quaternary upper ocean thermal gradient variations in the South China Sea: Implications for east Asian monsoon climate, *Paleoceanography*, *20*, PA4007, doi:10.1029/2004PA001115.
Timm, O., P. Köhler, A. Timmermann, and L. Menviel (2010), Mechanisms for the onset of the African humid period, *J. Clim.*, *23*(10), 2612–2633.
Timm, O., and A. Timmermann (2007), Simulation of the last 21,000 years using accelerated transient boundary conditions, *J. Clim.*, *20*, 4377–4401.
Timm, O., A. Timmermann, A. Abe-Ouchi, and T. Segawa (2007), On the definition of paleo-seasons in transient climate simulations, *Paleoceanography*, *23*, PA2221, doi:10.1029/2007PA001461.
Timmermann, A., F. Justino, F.-F. Jin, U. Krebs, and H. Goosse (2004), Surface temperature control in the North and tropical Pacific during the last glacial maximum, *Clim. Dyn.*, *23*, 353–370.
Timmermann, A., S. Lorenz, S.-I. An, A. Clement, and S.-P. Xie (2007), The effect of orbital forcing on the mean climate and variability of the tropical Pacific, *J. Clim.*, *20*, 4147–4159.
Timmermann, A., O. Timm, and L. Menviel (2009), The roles of CO2 and orbital forcing in driving southern hemispheric temperature variations during the last 21,000 years, *J. Clim.*, *22*, 1626–1640.
Troelstra, S., and D. Kroon (1989), Note on extant planktonic foraminifera from the Banda Sea, Indonesia (Snellius-II Expedition, cruise G5), *Neth. J. Sea Res.*, *24*, 459–463.
Uchikawa, J., B. Popp, J. Schoonmaker, A. Timmermann, and S. Lorenz (2010), Geochemical and climate modeling evidence for Holocene aridification in Hawaii: Dynamic response to a weakening equatorial cold tongue, *Quat. Sci. Rev.*, *29*, 3057–3066.
Wan, S., Z. Jian, X. R. Cheng, P. J. Qiao, and R. J. Wang (2010), Seasonal variations in planktonic foraminiferal flux and the chemical properties of their shells in the southern South China Sea, *Sci. China, Ser. D Earth Sci.*, *53*, 1176–1187.
Wang, Y. V., G. Leduc, G. Regenberg, N. Andersen, T. Larsen, T. Blanz, and R. R. Schneider (2013), Northern and Southern Hemisphere controls on seasonal sea surface temperatures in the Indian Ocean during the last deglaciation, *Paleoceanography*, *28*, 619–632, doi:10.1002/palo.20053.
Wejnert, K., C. Pride, and R. Thunell (2010), The oxygen isotope composition of planktonic foraminifera from the Guaymas Basin, Gulf of California: Seasonal, annual, and interspecies variability, *Mar. Micropaleontol.*, *74*, 29–37.
Wiesner, M., H. K. Wong, L. Zheng, Y. Wang, and W. Chen (1996), Fluxes of particulate matter in the South China Sea, in *Particle Flux in the Ocean*, edited by V. Ittekot et al., pp. 293–312, Wiley, New York.
Yoder, J., and M. Kennelly (2003), Seasonal and ENSO variability in global ocean phytoplankton chlorophyll derived from 4 years of SeaWiFS measurements, *Global Biogeochem. Cycles*, *17*(4), 1112, doi:10.1029/2002GB001942.
Ziveri, P., and R. Thunell (2000), Coccolithophore export production in Guaymas Basin, Gulf of California: Response to climate forcing, *Deep Sea Res. Part II*, *47*(9–11), 2073–2100.